Manuscript prepared for J. Name
with version 4.2 of the LaTeX class copernicus.cls.
Date: 14 August 2013

On the determination of gravity wave momentum flux from GPS radio occultation data

A. Faber[1,2], **P. Llamedo**[3], **T. Schmidt**[1], **A. de la Torre**[3], **and J. Wickert**[1]

[1]Department 1 Geodesy and Remote Sensing, GFZ German Research Centre for Geosciences, Potsdam, Germany
[2]Institute for Space Sciences, Freie Universität Berlin, Berlin, Germany
[3]Facultad de Ingeniería, Universidad Austral, Buenos Aires, Argentina

Abstract.

GPS Radio Occultation (RO) is a well-established technique for obtaining global gravity wave (GW) information. RO uses GPS signals received aboard low Earth orbiting satellites for atmospheric limb sounding. Temperature profiles are derived with high vertical resolution and provide a global coverage under any weather conditions offering the possibility for global monitoring of the vertical temperature structure and atmospheric wave parameters. The six satellites constellation COSMIC/FORMOSAT-3 delivers approximately 2000 temperature profiles daily. In this study, we use a method to obtain global distributions of horizontal gravity wave wavelengths, to be applied in the determination of the vertical flux of horizontal momentum transported by gravity waves. A method for the determination of the real horizontal wavelength from three vertical profiles is applied here to the COSMIC data. The horizontal and vertical wavelength, the specific potential energy (E_p) and the vertical flux of horizontal momentum (MF) are calculated and their global distribution is discussed.

1 Introduction

The important role of gravity waves (GWs) for atmospheric circulation and energy transport is already recognized (Nappo, 2002; Fritts and Alexander, 2003; Sutherland, 2010; M. Alexander et al., 2010). Recent developments in gravity wave effects and momentum flux analysis are summarized by M. Alexander et al. (2010). The variety of atmospheric sounding instruments, designed to detect GWs and find answers to related queries, has increased over the last decades. Radiosonde soundings, ground based measurements as well as air- and spaceborne measurements cover a large range of measuring possibilities. The two major measuring techniques for satellite measurements are: i) nadir-scanning instruments, like the Advanced Microwave Sounding Unit (AMSU)(Eckermann et al., 2006) or the Atmospheric InfraRed Sounder (AIRS) (Hoffmann and Alexander, 2009) and ii) limb-sounding instruments, like the CRyogenic Infrared Spectrometers and Telescopes for the Atmosphere (CRISTA) (Ern et al., 2004), the High Resolution Dynamics Limb Sounder (HIRDLS), the Sounding of the Atmosphere using Broadband Emission Radiometry (SABER) and the many radio occultation (RO) receivers aboard the different Low Earth Orbiting (LEO) satellites like the Constellation Observing System for Meteorology, Ionosphere and Climate (COSMIC) (see Wright et al., 2011). The GPS RO technique provides vertical profiles of atmospheric properties such as refractivity, from which density (ρ), pressure (P), temperature (T) and water vapor pressure (e) are derived. The vertical resolution of RO profiles ranges from 0.1 km in the lower troposphere to 1.4 km in the stratosphere (Kursinski et al., 1997). This technique operates under any weather conditions and provides a global coverage. However, the sampling of the GPS RO method is more irregular in time and space than other technique. A long term series of GPS RO measurements is available from the CHAllenging Minisatellite Payload (CHAMP) satellite, which had provided approximately 150 daily profiles between 2001 and 2008 (Wickert et al., 2001; Wickert, 2002). A higher density of data is given by COSMIC. The joint Taiwan/US science mission started in April 2006 and delivers approximately 2000 daily profiles (Anthes et al., 2008). RO receivers are also operating aboard of other satellite missions like the Gravity Recovery and Climate Experiment (GRACE, launched in 2002), or the two radar satellites TerraSAR-X (launched in 2007) and TanDEM-X (launched in 2010). The RO technique has been widely used for GW analysis (see Kuo et al., 2000; de la Torre and Alexander, 2005; P. Alexander et al., 2008a,b; Horinouchi and Tsuda, 2009; Lin et al., 2010; Wang

Correspondence to: A. Faber
(antonia.faber@gfz-potsdam.de)

and Alexander, 2010). As shown by Marquardt and Healy (2005), small scale fluctuations of dry temperature RO profiles can be interpreted as gravity waves (GWs), when the vertical wavelength is equal or greater than 2 km. For lower wavelengths the fluctuations may be related to noise. To keep the signal to noise ratio for the temperature fluctuation above the detection threshold, the analysis should be applied to altitudes lower than 30 km (P. Alexander et al., 2008a) or, as suggested by Marquardt and Healy (2005), in the 20-30 km altitude range. The mean specific potential energy (E_p) is a parameter for the characterization of gravity wave activity, given by

$$E_p(z) = \frac{1}{2}\left(\frac{g}{N_z}\right)^2\left(\frac{T'}{\overline{T}}\right)^2 \quad (1)$$

$$N_z^2 = \frac{g}{\overline{T}}\left(\frac{\delta\overline{T}}{\delta z} + \frac{g}{c_p}\right)$$

where N_z is the Brunt-Väisälä frequency, g is the gravitational acceleration, c_p the isobaric heating capacity and T' and $\overline{T}$ are the fluctuation and background components of temperature, respectively. Unlike planetary waves, small scale GWs are usually sub-grid scale phenomena or underresolved in both the horizontal and the vertical in numerical weather prediction models (M. Alexander et al., 2010). In order to quantify the effect of small scale GWs alone, it is important to separate these from planetary waves. The GW analysis is based on the extraction of the vertical T' contribution. Together with the measuring technique, the background determination sets the range of detectable GWs even though the amount of planetary waves can not be perfectly extracted. Here, a continuous wavelet transform (CWT) analysis is used for the background determination (see Sect.2.1).

Ern et al. (2004) introduced a method to derive horizontal wavelength (λ_h^p) projected along the line connecting two adjacent T profiles (using CRISTA temperature data), for a given altitude instead of:

$$k_h^p = \frac{\Delta\phi_{ij}}{\Delta x_{ij}} = \frac{2\pi}{\lambda_h^p} \quad (2)$$

where Δx_{ij} is the distance and $\Delta\phi_{ij}$ is the phase shift between the two profiles at a given altitude, respectively. To extract the true horizontal wavelength (λ_h) of the gravity wave, at least a third T profile is needed (not aligned with the others). Measurements must be close in time and space, to provide observations of the same wave packet. The absolute value of vertical flux of horizontal momentum ($\mathbf{MF}$), for mid frequency approximation and assuming a single prevailing wave within the packet, is given by

$$|MF| = \rho\frac{\lambda_v}{\lambda_h}E_p \quad (3)$$

where λ_v is the vertical wavelength. Wang and Alexander (2010) used clusters of three or more RO measurements grouped in 15° x 15° x 4 h (longitude x latitude x time) cells to derive λ_h and the MF in the altitude rage of 17.5-22.5 km during December 2006 to February 2007. This described method represents an overdetermined set of equations which is not optimized. In this paper, we apply the Wang and Alexander (2010) method for deriving λ_h from multiple profiles, but limit the results to only those derived from 3 profiles, and compute resulting GW parameters at a higher spatial resolution of 5° x 5° lat/lon. Other differences compared to Wang and Alexander (2010) are the phase shift ($\Delta\Phi$) limitations and restrictions regarding the geometric arrangement of the groupings (see Sects. 3 and 4).

In Sect.2 the GPS measuring technique and the processing of the data set (2.1) is described, section 3 focuses on the determination of the real horizontal wavelength. Sect. 4 shows sensitivity studies for the determination of λ_h and λ_h^p and Sect.6 presents the global distribution results of the GW parameters.

2 GPS RO Technique

A GPS receiver on board a LEO satellite measures the Doppler shift of the dual frequency signal of one of the many GPS satellites rising or setting on the local horizon. The Doppler shift can be converted to the radio wave bending angles from which the atmospheric refractivity is derived. In the neutral atmosphere, the refractivity is further reduced to temperature (T), pressure (P) and electron density in neutral atmosphere profiles (Anthes et al., 2008; Kursinski et al., 1997).

The capability of the RO technique to properly detect GWs depends principally on the relative orientation between the wave fronts and the line-of-sight (LOS) between the GPS and LEO satellites. Wave amplitudes can be better resolved when the fronts are nearly horizontal or when the angle between the LOS and the horizontal component of the wave vector approaches $\pi/2$ (P. Alexander et al., 2008a). Short horizontal scale waves have a high probability to be attenuated or not be detected at all. The geometry of gravity wave detection is further explained by Preusse et al. (2009). In opposite to CRISTA, the GPS RO data sets (indifferent of which mission) have neither a regular spanned grid on which the measurements are taken nor an almost constant LOS.

In this work we use the COSMIC post-processed dry temperature profiles provided by the UCAR COSMIC Data Analysis and Archival Center (COAAC) Version 2007.3200 for the global analysis. The dry temperature profiles are provided from near the surface up to 40 km, at 0.1 km steps.

2.1 Data Processing

In order to calculate E_p, the fluctuation has to be extracted from each T profile. Earlier works (Hocke and Tsuda, 2001; Tsuda et al., 2000, 2004; Baumgaertner and McDonald, 2007; de la Torre et al., 2006a,b; Schmidt et al., 2008)

used a vertical filter directly on the T profile. The resulting T' profiles ($T' = T - \overline{T}$) still include longer waves with vertical wavelengths (λ_v) similar to GWs (e.g., Kelvin waves Holton et al., 2001). To exclude planetary and Kelvin wave contribution, a $\overline{T}$ including these waves must be computed. Following closely Wang and Alexander (2009, 2010) we first binned all T profile data (taking into account a compromise between the resolution that we may obtain and the density of available profiles) into a 10° x 15° lat/lon field between 9-40 km with a vertical resolution of 100 m. For the daily binned profiles, a CWT as a function of longitude is performed, for each latitude and altitude. This allows to estimate wave numbers 0-6 for each longitude. The "large scale variation", reconstructed by wave numbers 0-6 are then interpolated back onto the location of the original T profile and subtracted from it. The resulting T' represents the wave fluctuations of short scale waves (shorter than wave number 6). For this determination of $\overline{T}$ time variations of large-scale waves within 1 day are not taken into account.

Then λ_v (using a CWT analysis) and E_p (using (1)) can be directly computed from the T' profiles and are later presented as seasonal mean values in a 5° x 5° resolution. From (2), λ_h^p along the line connecting two adjacent T profiles for a given altitude is determined. The method is restricted to pairs of measurements within a small temporal and spatial window (both measurements are supposed to be taken within the same π-cycle of the wave). To ensure the same wave packet, the vertical structure of the considered profiles must be similar. For the phase difference determination, it is very important that all the RO profiles are measured with a similar LOS. In ideal case, the LOS of all the measurements are parallel. In addition to that, the geometric configuration between the LOS and the wave propagation direction limits the capability to see a GW (P. Alexander et al., 2008a). Using at least three RO measurements (not collinear with each others), we can derive λ_h instead of λ_h^p. All RO profiles of these groupings must fulfill strict temporal and spatial restrictions. In this work the temporal and spatial windows were set to 2 h and 15° in all directions. The reason for these parameter settings will be explained in Sect.4.

P. Alexander and de la Torre (2010) used a similar method to derive wavelengths in a Cartesian coordinate system from three soundings. They describe that the ideal case would be a perpendicular arrangement between the three soundings, but the COSMIC constellation does not provide these ideal cases.

The six identical COSMIC satellites were launched on one rocket into an orbit of 405 km and later on raised to their final orbit of approximately 800 km. During the COSMIC clustering phase (the first months) several measurements were obtained in a small spatial and temporal window and with similar LOS.

Before this method is applied to the RO data, the relative positioning of pairs of RO profiles with respect to the wave must be taken into account. In the case that the alignment of one of the pairs is perpendicular to the wave propagation direction, the T' profiles will not have a phase shift between each other. Those pairs of RO measurements where $\Delta\Phi$ is lower than 0.5 radian ($\lambda_h^p >$ 10,000 km) are not taken into account (see Sect.4).

From the CWT analysis (using a Morlet wavelet) the dominant λ_v at considered altitudes is determined. We treat T' profiles with a dominant λ_v within an interval of 2 km as they belong to the same wave system. The analyzed vertical wavelength interval ranges between 2 and 12 km, therefore the vertical wavelength window is chosen rather small. Ern et al. (2004) used a window of 6 km for the CRISTA-2 data set. In Fig. 1a, two RO temperature profiles ($T_{1,2}$) are displayed for the altitude range between 20-30 km. Their global (for the entire altitude range) dominant (λ_v) is shown in Fig. 1b for T_1 and 1c for T_2. The cross-wavelet spectrum (Fig. 1d) shows the amplitudes of the dominant λ_v at each altitude. This is needed for the phase shift determination at each altitude between all pairs of T profiles. Once the phase shift and the distances are known, k_h^p can be derived for all altitudes.

3 Horizontal Wave Parameters

For the MF determination, we need k_h instead of k_h^p. As mentioned before, a third measurement is needed to derive k_h. For a detailed explanation we take a look at Fig. 2, starting with 2a. Two vertical T' RO profiles ($T'1$ in brown and $T'2$ in blue), separated by the horizontal distance Δx are displayed. The $\Delta\Phi$ between these measurements is derived from a cross wavelet analysis for each altitude. Fig. 2b shows the derived k_h^p (orange arrow) from three T' measurements at one altitude and the true k_h (green arrow). The dotted lines are the corresponding λ_h^p (orange line) and λ_h (green line). When using these three measurements, k_h can be derived by:

$$\Delta\phi_{ij} = k(x_i - x_j) + l(y_i - y_j) \qquad i,j = 1,2,3 \qquad (4)$$
$$k_h = \sqrt{(k^2 + l^2)}$$

where (k,l) are the horizontal components of the wave number vector, and ($x_{i,j}$, $y_{i,j}$) are the RO coordinates at given altitude. This equation is also the basis of the least square fitting method which Wang and Alexander (2010) used to determine the horizontal wavelength. Here, derivation of the horizontal wavelength is derived using alway only three measurements, thus avoiding an over determination of the problem and so optimizing the available limited information, given the considerably sparse data density. $\Delta\Phi_{ij}$ is derived from cross wavelet analysis for each pair of T' profiles (Fig. 2c). Since this is an over-determined problem, there can be more than one result. The reference point (RP) from which this system of equations is solved, plays an important role. As shown in Fig. 2c, the location of (x_{ij},y_{ij}) and the distances between the points (Δx_{ij}) are known as well as the phase shifts ($\Delta\Phi_{ij}$) between each measurement pair. When using P1 as RP, then (4) is solved using two equations for

Δx_{ij}: Δx_{12} and Δx_{13}). In a similar way, P2 as RP Δx_{ij} are Δx_{12} and Δx_{23} and for P3 as RP Δx_{ij} are Δx_{13} and Δx_{23}. When solving the equations for each RP, three k_h are derived. As displayed in Fig. 2d at least two identical k_h (green arrows) and a third k_h (purple arrow) are derived. All three displayed green arrows are identical in lengths and orientations. The two starting in P1 and P3 represent the computed wave vectors, the third green arrow is shifted to fit the phase maximums of the background wave. The inconsistent k_h can be different from the two identical k_h in both, orientation as well as length of k_h, but it might also be identical to the two others. This depends on the angles between the three measuring points as explained below. When taking a look at the wave fronts the reason for the wrong determination of k_h at one RP becomes more clear. The RP that produces the non consistent result is placed in between the other two points regarding the wave fronts.

Another way to treat this problem is a geometric description as presented in Figs.3 and 4. Considering the same three points as before, representing the intersection of three closely separated RO profiles with a constant altitude plane. The unknown constant successive wave phase lines Φ and $\Phi \pm 2\pi$ are illustratively shown in Fig. 3a. The line of action (line ab), as well as the direction of k, are obviously also unknown. Now, the three possible pairs of points, as shown in Figs.3b, c and d are considered. The slope of k_h may be determined, for example in the case shown in Fig. 3b, in the following way: From (2) and the knowledge of both the phase and distance differences between each pair of points, λ_h^p (black sinusoidal lines) may be determined (Fig. 4a). If now we displace these curves along the blue lines defined by each pair, until matching a common extreme (red sinusoidal curves), the opposite extremes of these red curves define the slope of Φ (line cd). We repeat this procedure in Fig. 4b, observing identical result. In the case of (Fig. 4c), note that one of the black curves was displaced in the opposite direction, in order to be able to obtain the same slope as in the precedent two cases. The displacement to the side of the second point (like in the other two cases) would lead to the gray line ef with a slope that does not match the results from the two reference points before (brown and yellow point, Figs.4a and b). The displacement along the alignment of the blue and brown point leads to the blue line cd, which matches the results from before. This happens, when one of the inner angles α,β or γ (in Fig. 3a) is an obtuse angle. If the three angles are acute, no inversion is needed and the three possibilities described, render straightforwardly an identical result. In general, for practical purposes and to handle a huge amount of groupings of three points, after computing the phase slope as in Figs.4a to c for each 3-point grouping, no possible uncertainty remains if we simply consider the prevailing slope (to include 3-point groupings with one inner obtuse angle). λ_h is finally illustrated in Figs.4a-c (green curves). When evaluating the phase differences, inconsistencies may arise from wraparound effects. Depending on the reference point, due to the periodicity of the problem, the same phase difference could be regarded, for example, as either very small, or close to 2π. Also the inner angle at the reference point must be obtuse to determine a valuable horizontal wavelength. These effects are accounted for by evaluating all possible combinations of a considered group of three points and sorting out the inconsistent combinations.

4 Sensitivity Study

As mentioned in Sect. 1 the temporal window should be kept as small as possible, still allowing a sufficient number of 3-point groupings to extract global distributions of the wave parameters. We choose a 2 h interval. Shorter windows would decrease the number of possible groupings of 3-points too much, whereas a larger time window would increase the number of 3-points, but this would also include profiles from different wave origin. For a closer look, we apply a sensitivity study to (2), using two sinusoidal curves with different phase shifts (0° and 180°) and four horizontal distances (100, 200, 500 and 1,000 km). This only focuses on the one-dimensional case (on λ_h^p). With a decreasing phase shift, λ_h approaches very high values (Fig. 5). This effect is even stronger when Δx increases. A detection of small phase shifts (lower than 30°) shows for all distances very long wavelengths ($\lambda_h^p \to \infty$). For larger distances (for example 1,000 km), a phase shift of 45° corresponds to a λ_h^p of more than 10,000 km. These long λ_h are unrealistic for GWs. This and the fact, that alignments cannot be ruled out (small phase shift at a given altitude might be due to the $\pm 2\pi$ or even $\pm 3\pi$ periodicity), leading to a limitation of the phase shift. Therefore we set a lower limit of 0.5 radian ($\sim 30^\circ$), when additionally the maximum distance is set to be 15°. The new limiting factor must be taken into account when using this method to analyze GPS RO profiles.

Now we take a look on the impact of the distance dependence for the λ_h determination using (4) (the two-dimensional case). Triads with the spatial interval of 5°, 10° and 15° were identified. The first and obvious result is that the shorter the interval, the less 3-point groupings can be found. This was performed for the northern hemisphere (NH) winter 2006/07 for the altitude range 20-30 km. For 5° the amount of 3-points is too small for a sufficient statistical global analysis. The results for 10° and 15° are shown in Fig. 7. Although the absolute values vary by approximately 50%, the structure of λ_h is quite similar for both settings. The same effect can be found when studying the results for the MF distribution. A more detailed description of λ_h and MF is given in Sect.6. The fact, that the horizontal wavelength is strongly dependent on the maximum distance limit shows, that the global distribution of gravity wave horizontal wavelengths cannot ne reliably determined with the large distances required to obtain sufficient statistics. This method can provide λ_h only as an upper boundary due to

alignment effects and limitations in the measuring principles and data availability. The 15° horizontal spacing for the 3-points search was chosen for the global analysis. In addition, the data availability does not allow a global analysis for NH summer with a 10° interval.

5 Comparison 2-point verses 3-point method

As a reference, that the 3-point method works right, the results of the horizontal wavelength should always be shorter then those derived by the 2-point method from Ern et al. (2004). Therefor the determination of λ_h^p and the true λ_h is shown in Fig. 6a and b for a 10° spacing and the λ_h^p for a < 300 km spacing in Fig. 6c. Corresponding to these horizontal wavelengths, the momentum flux is displayed in Fig. 6d-f. First the comparison for the 10° spacing is discussed (Fig. 6a and b). Th detected projected (a) and true (b) horizontal wavelength show clearly, that the 3-point method decreases the horizontal wavelength. The 2-point method delivers wavelengths between 3000 and 5000 km, whereas the 3-point method with the same spacing decreases the detected wavelengths down to values between 1000 and 2500 km. This effect of detecting shorter wavelengths is also found, when decreasing the spacing for the 2-point method down to a maximum value of 300 km (Fig. 6c). Here the determined projected wavelengths vary between 2000 and 5000 km. This states clearly, that even though the spacing of 15° is rather big, the results are more realistic than those from the 2-point method. For the momentum flux, the determined horizontal wavelength plays an important role. The detection of shorter wavelengths leads to higher values in the momentum flux distribution. Therefore the results from the 3-point method (Fig. 6e) show higher values than those of the 2-point method with both spacings (10° and < 300 km in Figs. 6d and f, respectively).

6 Global Analysis

For a global analysis, seasonal mean data for June - August 2006 (JJA) and December 2006 - February 2007 (DJF) are shown. The altitude range for the statistical analysis is set to 20-30 km. The global distribution of the number of available 3-point groupings and their mean distance between each 3-points are shown in Fig. 8 for the NH summer (a,c) and winter (b,d) respectively. Fig. 8a and b show, that the number of 3-points are higher in the extra tropics than in the equator region or closer to the poles. As mentioned in Sect. 4, the amount of measurements in the beginning of the COSMIC mission was not as high as expected. By the end of 2006 all six satellites were running and therefore increasing the number of ROs. For Figs. 8a and b, different scales are chosen to see the structure of the grouping of 3-points for both seasons. The mean distance of the 3-points (see Fig. 8c and d) is similar, but the clustering phase of the beginning of the COSMIC mission has a small impact which leads to shorter distances for the NH summer than winter. These differences are most distinct over Australia and Southern America. The maximum distance is limited by a 15° circle, which represents about 1500 km at the equator and 500 km at high latitudes. The gaps in the NH summer are found in all wave parameters. There, the number of the 3-point groupings is too small for a statistical analysis. For all wave parameters, as well as for the mean distance, the results of each 3-points (mean E_p, λ_v and the computed λ_h along with MF) are attributed to their mean lat/lon position (MP) and then fed into a 5°x 5° lat/lon grid. Due to the low numbers of 3-points in polar regions (north of 75°N, south of 75°S) these areas are not evaluated. As mentioned before, a temporal and spatial window is used, the $\Delta\Phi$ limitation and the comparison of the dominant λ_v eliminate about 30 % of all measured 3-points.

Figs.9a and b display the λ_v distributions for NH summer (a) and winter (b) with values of minimum 5 km around the equator and up to 10 km in the extra tropics and polewards. At first sight, a small general decrease of λ_v from 9a to b can be seen. Taking a closer look, some significant changes in both directions are detectable. For example the decrease of λ_v over Canada and the US as well as over Russia from about 9 km down to less than 7 km or the increase of λ_v over Australia and north Africa. All these changes are located over land, but there is also a decrease in the λ_v over the southern hemisphere (SH) water regions, which is most significant around the Antarctic Peninsula.

The E_p distribution (see Figs.9c and d) agree with previous results (Schmidt et al., 2008). The higher values (up to 5 J/kg) are located along the equator for both seasons and decrease towards the polar regions. However for Jun. - Aug. 2006 the higher values in the extra tropics are located on the SH, with explicit high values along the east side of the Andes mountains mainly due to low level westerlies and the permanent jet (P. Alexander and de la Torre, 2010). For Dec. 2006 - Feb. 2007 higher values are found in the NH. Going from west to east, the increase in E_p in the NH can be explained by the various mountain chains and wind shear conditions. East of northern America, and in the north east of Russia, the NH winter weather conditions provide strong wind shear. In northern Europe, the prevailing westerlies induces GWs on the lee side of the Scandinavian mountains with values of up to 5 J/kg. The subtropical jet stream induces hight values of E_p when crossing the Zagros Mountains (Farajzadeh et al., 2011). For both seasons, the equator region shows high E_p values around 4 J/kg. These values are due to the high amount of convective potential from high temperatures and humidity in that area.

The λ_h distributions, see Figs.10a for JJA and 10b for DJF, show a trend of increasing λ_h towards the equator. The reason for the different starting point of the λ_h scale is the visibility of the pattern requires different scales for each graphic. This kind of pattern has already been shown by Fröhlich et al. (2007), who used a theoretical λ_h, and by Wang and Alexan-

der (2010) using GPS RO data. Also, the λ_h distribution shows longer λ_h over water on the winter hemispheres than on the summer hemisphere and decreasing λ_h over the winter hemisphere land areas compared to the same regions in summer. For the SH winter (Fig. 10a) the effect of shorter wavelength over land is most significant. The absolute value of λ_h at the east of the Andes is higher than the results from de la Torre and Alexander (2005), but the here derived λ_h is only an upper boundary of λ_h (see Sect.4). The λ_h would decease by a mean of 50% when changing the spatial window from 15° to 10°.

The global MF distribution is displayed in Figs.10c and d for JJA and DJF respectively. The absolute values of MF range between 0.2 and 1.7 mPa, but the pattern of the distribution is more crucial for the evaluation. The absolute values depend on the derived λ_h and therefore also in the chosen spatial interval. For the MF however, the absolute values increase when choosing a shorter spatial window, but the pattern does not change significantly. For both seasonal mean MF distributions (JJA and DJF), a band of high values is located along the equator. Additional to that, the winter hemisphere shows more wave activity (higher MF values) than the summer hemispheres. The higher values are found at the east of the Andes mountains and along the Antarctic Peninsula during the SH winter (Fig. 10c) and at the east on the Scandinavian mountains and the Zargos mountains (Iran) during the NH winter (Fig. 10d).

MF derived from model data and satellite measurements are performed by Geller et al. (2013). Other global distributions of the MF were given, e.g., by Ern et al. (2004, 2011); Fröhlich et al. (2007); Wang and Alexander (2010). Again, the absolute values shall not be compared even though the range is in the 0.2 to 1.2 mPa fits the results derived by Ern et al. (2004) and Fröhlich et al. (2007). But the general patterns fit each other as well. Not all results are presented for both seasons and for that exact time period, therefore the patterns can also differ. But all results show higher values of MF on the winter hemisphere. Wang and Alexander (2010) show also the two spots over southern America and Africa for the same time period (DFJ) and the high MF over Scandinavia. The method of taking 3-points instead of a fixed 15° x 15° grid, allows a higher resolution in the final distributions of the derived wave parameters.

7 Conclusions

This study provides information about the determination of momentum flux using three co-located RO profiles. COSMIC data from the clustering phase (April 2006 - Feb. 2007) were analyzed. Some of the limitations applied come from the method introduced by Ern et al. (2004) (small temporal and spatial windows, analysis for each altitude), others were added to minimize the alignment effects (λ_v, $\Delta\Phi$ and E_p). Global distributions of the vertical, horizontal wavelength as well as potential energy and MF as seasonal means in the altitude range 20 to 30 km, from Jun. - Aug. 2006 and Dec. 2006 - Feb. 2007 are displayed as an example of our studies. Wang and Alexander (2010) concluded, that the data density is rather too coarse for an accurate determination of the horizontal wave parameters. This work optimizes the approach of Wang and Alexander (2010), leading to results with a higher resolution. The new applied phase shift limitation and the restrictions in the geometric constellation of the regarded 3-points lead to a higher resolution in the results than Wang and Alexander (2010) showed. However, a disadvantage of this method is the high dependency of λ_h on the spacing within the 3-points. After the clustering phase of the six COSMIC satellites, the occultations were further apart making it harder to find suitable 3-points. But, the method can be applied to other vertical temperature measurements, as long as they provide the required spatial and temporal resolution.

Acknowledgements. Thanks to UCAR for providing the COSMIC data.

References

Alexander, M. J., M. Geller, C. McLandress, S. Polavarapu, P. Preusse, F. Sassi, K. Sato, S. Eckermann, M. Ern, A. Herzog, Y. Kawatani, M. Pulido, T. A. Shaw, M. Sigmond, R. Vincent, and S. Watanabe, Recent developments in gavity-wave effects in climate models and the global distribution of gravity-wave momentum flux from observations and models, Q. J. R. Meteorol. Soc. 136, 1103-1124, doi:10.1002/qj.637, 2010

Alexander, P., A. de la Torre, and P. Llamedo, Interpretation of gravity wave signatures in GPS radio occultations, J. Geophys. Res., 113, D16117, doi:10.1029/2007JD009390, 2008a

Alexander, P., and A. de la Torre, A Method to Infer Three Cartesian Wavelength of a Mountain Wave from Three Soundings, Am. Meteorol. Soc. Notes and Correspondence, 2069-2074, doi:10.1175/2010JAMC2348.1, 2010

Alexander, S. P., T. Tsuda, and Y. Kawatani, COSMIC GPS Observations of the Northern Hemisphere winter stratospheric gravity waves and comparisons with an atmospheric general circulation model, Geophys. Res. Lett., 35, L10808, doi:10.1029/2008GL033174, 2008b

Anthes, R. A., P. A. Bernhardt, Y. Chen, L. Cucurull, K. F. Dymond, D. Ector, S. B. Healy, S.-P. Ho, D. C. Hunt, Y.-H. Kuo, H. Liu, K. Manning, C. Mccormick, T. K. Meehan, W. J. Randel, C. Rocken, W. S. Schreiner, S. V. Sokolovskiy, S. Syndergaard, D. C. Thompson, K. E. Trenberth, T.-K. Wee, N. L. Yen, and Z. Zen, The COSMIC/Formosat-3 Mission Early Results, Am. Met. Soc., doi:10.1175/BAMS-89-3-313, 2008

Baumgaertner, A. J. G., and A. J. McDonald, A gravity wave climatology for Antarctica compiled from Challenging Minisatellite Payload/Global Positioning System (CHAMP/GPS) radio occultations, J. Geophys. Res., 112, D05103, doi: 10.1029/2006JD007504, 2007

de la Torre, A., and P. Alexander, Gravity waves above Andes detected from GPS radio occultation temperature pro-

files: Mountain forcing?, Geophys. Res. Lett., 32, L17815, doi:10.1029/2005GL022959, 2005

de la Torre, A., T. Schmidt, and J. Wickert, A global analysis of wave potential energy in the lower stratosphere derived from 5 years of GPS radio occultation data with CHAMP, Geophys. Res. Lett., 33, L24809, doi:10.1029/2006GL027696, 2006a

de la Torre, A., P. Alexander, P. Llamedo, C. Menendez, T. Schmidt, and J. Wickert, Gravity waves above the Andes detected from GPS radio occultation temperature profiles: Jet mechanism?, Geophys. Res. Lett., 33, L248010, doi:10.1029/2006GL027343, 2006b

Eckermann, S. D., D. L. Wu, J. D. Doyle, J. F. Burris, T. J. McGee, C. A. Hostetler, L. Coy, B. N. Lawrence, A. Stephens, J. P. McCormack, and T. F. Hogan, Imaging gravity waves in lower stratospheric AMSU-A radiances, Part 2: Validation case study, Atmos. Chem. Phys., 6, 3343-3362, doi:10.5194/acp-6-3343-2006, 2006

Ern, M., P. Preusse, M. J. Alexander, and C. D. Warner, Absolute values of gravity wave momentum flux derived from satellite data, J. Geophys. Res., 109, 1-17, doi:10.1029/2004JD004752, 2004

Ern, M., P. Preusse, J. C. Gille, C. L. Hepplewhite, M. G. Mlynczak, J. M. Russel III, and M. Riese, Implications for atmospheric dynamics derived from global observations of gravity wave momentum flux in stratosphere and mesosphere, J. Geophys. Res., 116, D19107, doi: 10.1029/2011JD015821, 2011

Farajzadeh, M., A. Khorany, and H. Lashkary, The Relation Between Jet Stream Location and Cyclones Over the Western Iran, Am. J. Applied Sci. 5 (10): 1308-1312, doi: 10.3844/ajassp.2008.1308.1312 2008

Fritts, D. C., and M. J. Alexander, Gravity wave dynamics and effects in the middle atmosphere, Rev. Geophys., 41(1), 1-64, doi:10.1029/2001RG000106, 2003

Fröhlich, K., T. Schmidt, M. Ern, P. Preusse, A. de la Torre, J. Wickert, and Ch. Jacobi, The global distribution of gravity wave energy in the lower stratosphere derived from GPS data and gravity wave modelling: Attempt and challenges, J. Atmos. Solar-Terr. Phy., 69, 2238-2248, doi:10.1016/j.jastp.2007.07.005, 2007

Geller, M. A., M. J. Alexander, P. T. Love, J. Bacmeister, M. Ern, A. Hertzog, E. Manzini, P. Preusse, K. Sato, A. Scaife, and T. Zhou, A comparison between gravity wave momentum fluxes in observations and climate models, J. Climate, in press, doi:10.1175/JCLI-D-12-00545.1, 2013

Hocke, K., and T. Tsuda, Gravity Waves and Ionospheric Irregularities over Tropical Convection Zones observed by GPS/MET Radio Occultation, Geophys. Res. Lett., 28, 2815-2818, doi:10.1029/2001GL013076, 2001

Hoffmann, L., and M. J. Alexander, Retrieval of stratospheric temperatures from Atmospheric Infrared Sounder radiance measurements for gravity wave studies, J. Geophys. Res., 114, D07105, doi:10.1029/2008JD011241, 2009

Holton, J. R., M. J. Alexander, and M. T. Boehm, Evidence for short vertical wavelength Kelvin waves in the Department of Energy-Atmospheric Radiation Measurements Nauru99 radiosonde data, J. Geophys. Res., 106, 20, 125-20, doi:10.1029/2001JD900108, 2001

Horinouchi, T., and T. Tsuda, Spatial structures and statistics of atmospheric gravity waves derived using a heuristic vertical cross-section extraction from COSMIC GPS radio occultation data, J. Geophys. Res., 114, D16110, doi:10.1029/2008JD011068, 2009

Kuo, Y.-H., S. Sokolovskiy, R. A. Anthes, and F. Vandenberghe, Assimilation of GPS Radio Occultation Data for Numerical Weather Prediction, Terr., Atmos. and Oceanic Sci., 11(1), 157-186, 2000

Kursinski, E. R., G. A. Hajj, J. T. Schofield, R. P. Linfiled and K.R. Hardy, Observing Earth's atmosphere with radio occultation measurements using the Global Positioning System, J. Geophys. Res., 102, 23, 429-23, doi:10.1029/97JD01569, 1997

Lin, L., X. Zou, R. Anthes, and Y.-H. Kuo, COSMIC GPS Radio Occultation Temperature Profiles in Clouds, Am. Met. Soc. MWR, 138, 1104-1118, doi:10.1175/2009MWR2986.1, 2010

Marquardt, C., and S.B. Healy, Measurement Noise and Stratospheric Gravity Wave Characteristics obtained from GPS Occultation Data,J. Met. Soc. Japan, Vol. 83, No. 3, 417-428, 2005

Nappo, C. J., An Introduction to Atmospheric Gravity Waves, *Academic Press Inc*, International Geophysics Serious, Vol. 85, 2002

Preusse, P., Schroeder, S., Hoffmann, L., Ern, M., Friedl-Vallon, F., Oelhaf, H., Fischer, H., and Riese, M.: New perspectives on gravity wave remote sensing by spaceborne infrared limb imaging, Atmos. Meas. Tech. Discuss., 2, 825-856, doi:10.5194/amtd-2-825-2009, 2009

Schmidt, T., A. de la Torre, and J. Wickert, Global gravity wave activity in the tropopause region from CHAMP radio occultation data, Geophys. Res. Lett., 35, L16807, doi:10.1029/2008GL034986, 2008

Sutherland, B. R., Internal Gravity Waves, Cambridge University Pres., 2010

Tsuda, T., M. Nishida, C. Rocken, and R. H. Ware, A global morphology of gravity wave activity in the stratosphere revealed by the GPS occultation data (GPS/MET), J. Geophys. Res., 105, 7257-7273, doi:10.1029/1999JD901005, 2000

Tsuda, T., M. V. Ratnam, P. T. May, M. J. Alexander, R. A. Vincent, and A. MacKinnon, Characteristics of gravity waves with short vertical wavelengths observed with radiosonde and GPS occultation during DAWEX (Darwin Area Wave Experiment), J. Geophys. Res., 109, D20S03, doi:10.1029/2004JD004946, 2004

Wang, L., and M. J. Alexander, Gravity Wave activity during stratospheric sudden warmings in the 2007-2008 Northern Hemisphere winter, J. Geophy. Res., 114, D18108, doi: 10.1029/2009JD011867, 2009

Wang, L., and M. J. Alexander, Global Estimates of Gravity Wave Parameters from GPS Radio Occultaton Temperature Data, J. Geophy. Res., 115, D21122, doi:10.1029/2010JD013860, 2010

Wicker, J., C. Reigberg, G. Beyerle, R. König, C. Marquardt, T. Schmidt, L. Grunwaldt, T. K. Meehan, W. G. Melbourne, and K. Hocke, Atmosphere sounding by GPS radio occultation: First results from CHAMP, Geophys. Res. Lett.,28(17), 3263-3266, doi:10.1029/2001GL013117, 2001

Wickert, J., Das CHAMP-Radiookkultationsexperiment: Algorithmen, Prozessierungssystem und erste Ergebnisse, Sci. Tech. Report STR 0207, GFZ, Potsdam, bib.gfz-potsdam.de/pub/str0207, 2002

Wright, C. J., , M. B. Rivas, and J. C. Gille, Intercomparisons of HIRDLS, COSMIC and SABER for the detection of stratospheric gravity waves, Atmos. Meas. Tech., 4, 1581-1591, doi:10.5194/amt-4-1581-2011, 2011

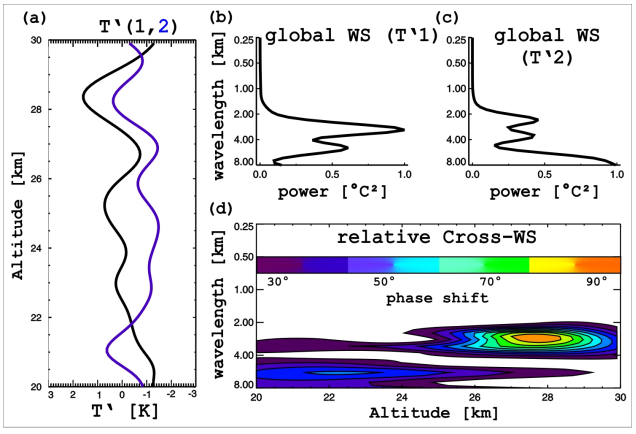

Fig. 1. Two RO temperature fluctuation profiles (a) and their corresponding horizontal wavelength (λ_v) spectrum (b,c). The cross-wavelet shows the amplitude at each altitude (d), for the dominant vertical wavelength (λ_v).

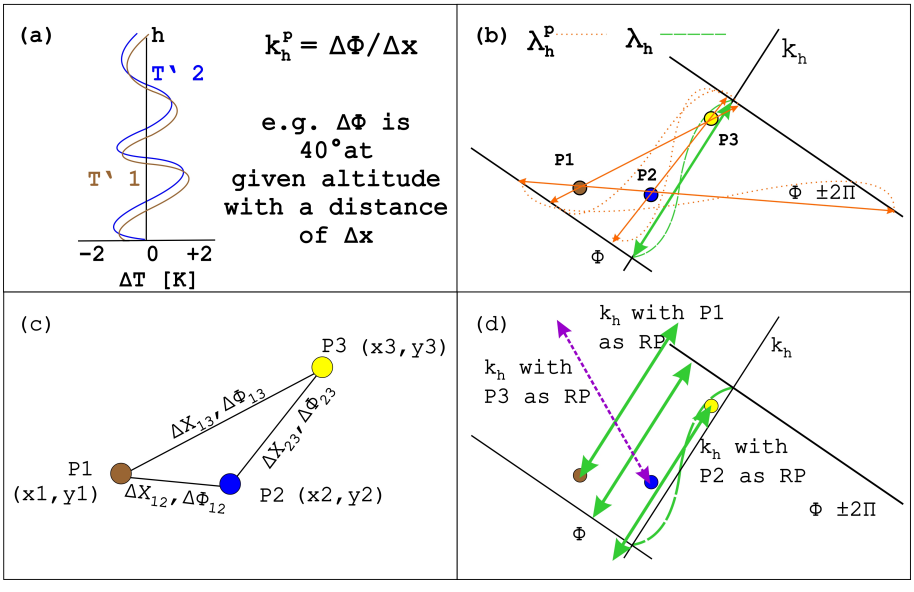

Fig. 2. Displayed are two vertical temperature profiles with a phase shift of 40° (a), the projected and real horizontal wavelet within a 3-points of measurements when the corresponding horizontal wave is known (b), the 3-points of measurements and the well-known parameters (c) and the three possible derived horizontal wave vectors for that 3-points (d). For explanations, see text.

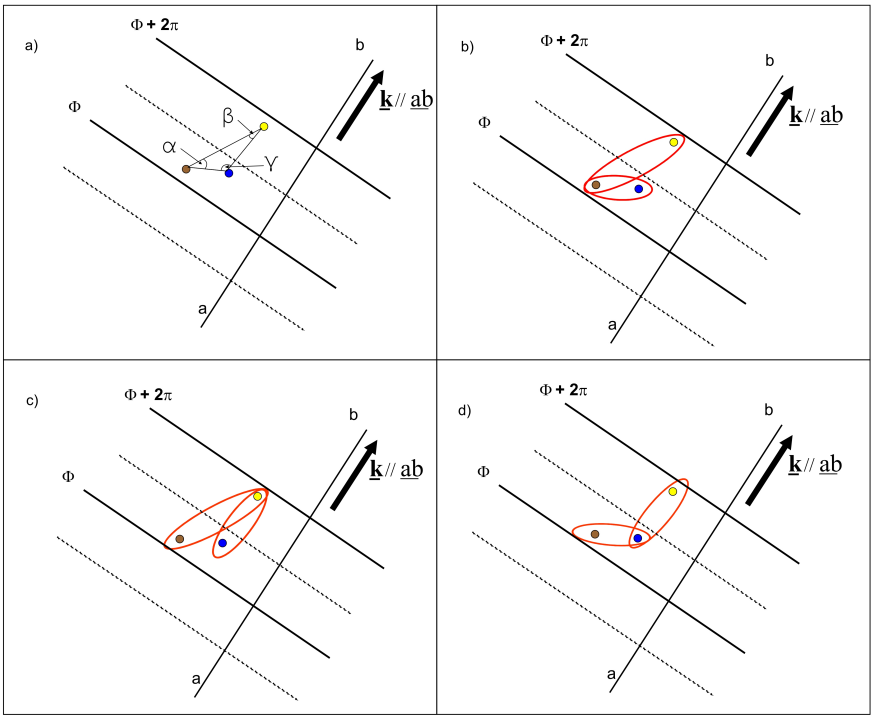

Fig. 3. Part A of the geometrical description of the determination of the real horizontal wavelength. Here the setup of the 3-points (a) and the three possible combinations of solving Equation 2 for different reference points (b, c and d) are displayed.

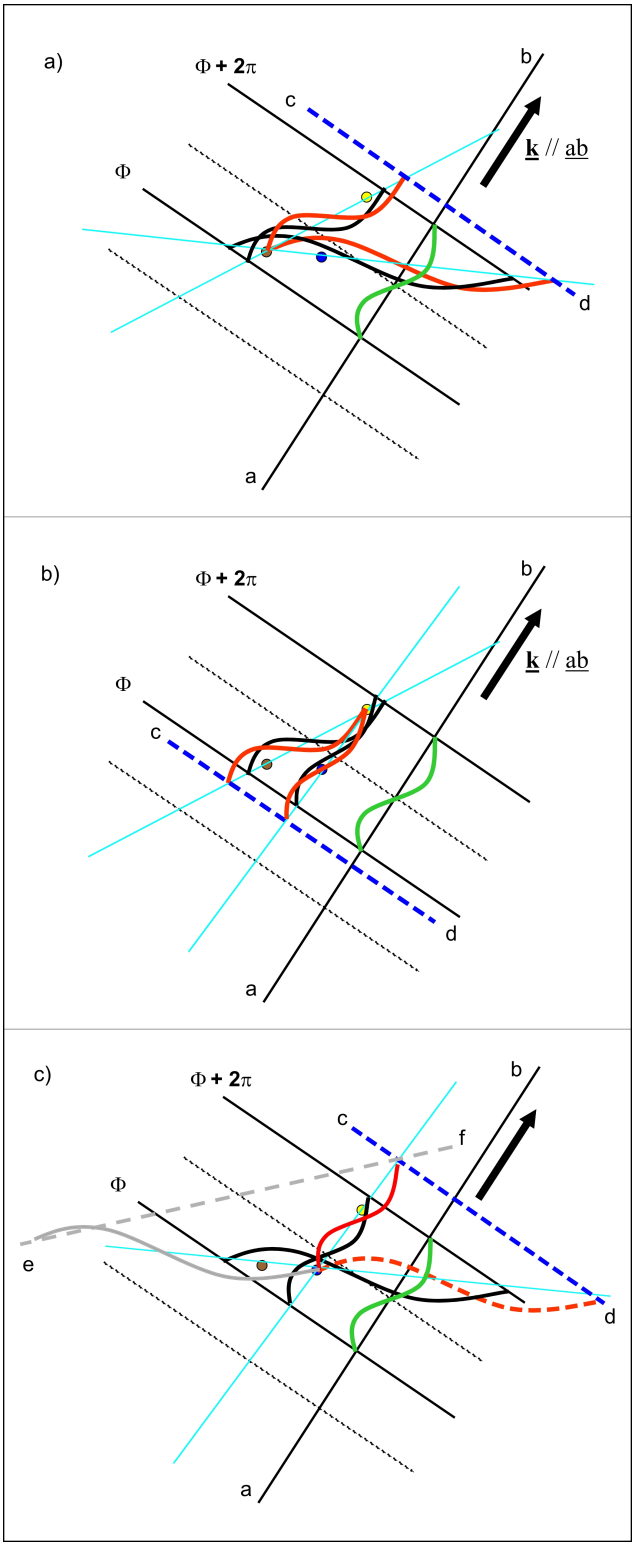

Fig. 4. Part B of the geometrical description of the determination of the real horizontal wavelength. The derived horizontal wavelength for each reference point (for Part A(b) is displayed in (a), for Part A(c) in Fig. (b) and for Part A(d) in Fig. (c).

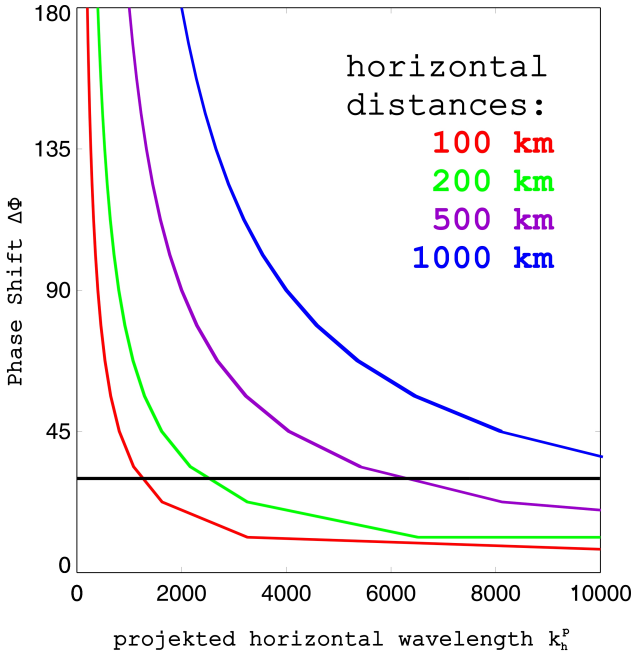

Fig. 5. Sensitivity study for the method introduced by Ern et al. (2004) concerning the resulting wavelength (k_h^p) at different horizontal distances and phase shifts.

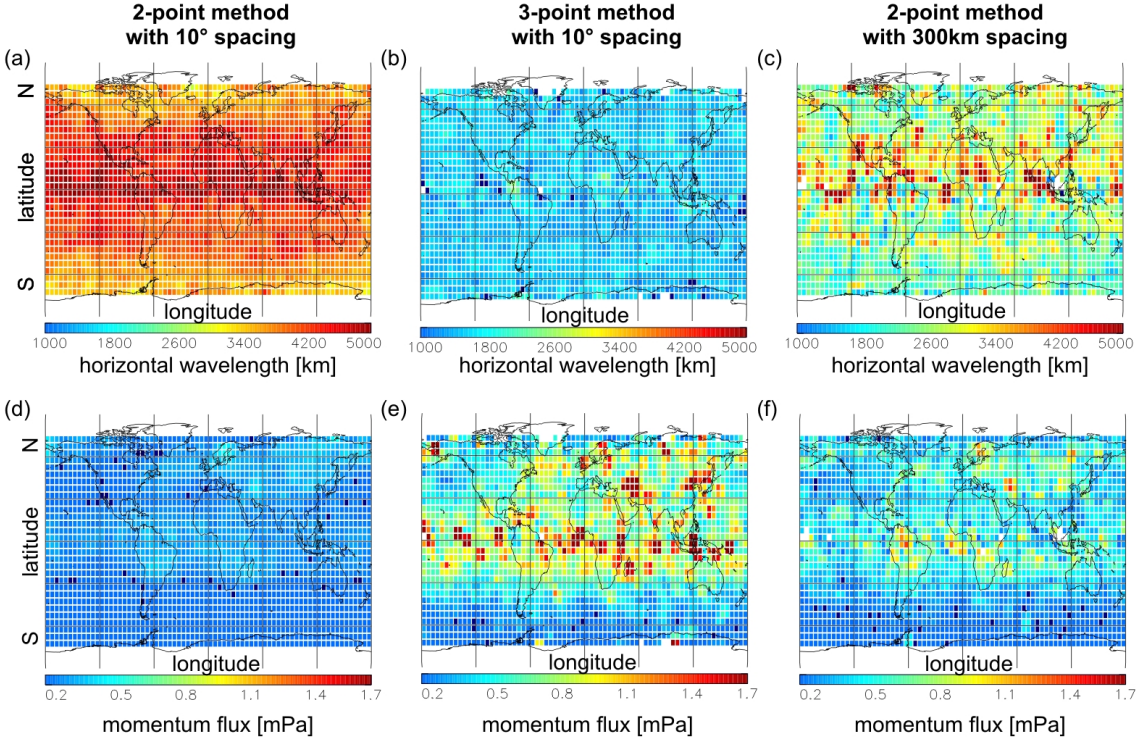

Fig. 6. Horizontal wavelength (k_h^p) (a and c) and true horizontal wavelength (b) with spacings of 10° (a and b) and < 300 km (c) and the corresponding momentum flux d-f.

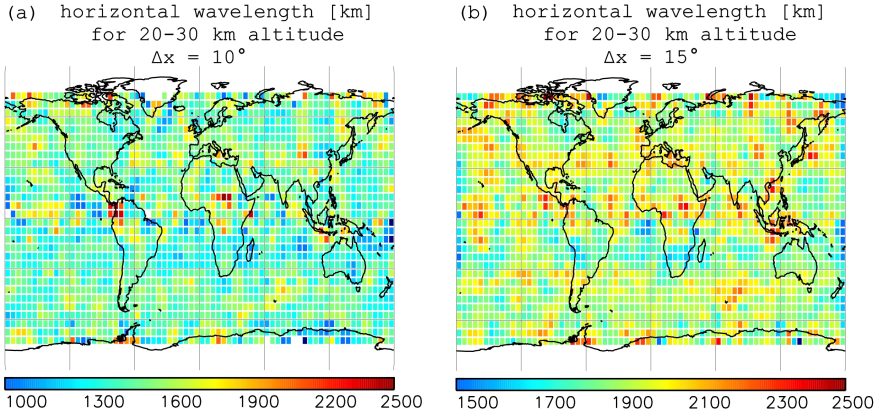

Fig. 7. Horizontal wavelength derived from 3-points of COSMIC RO temperature profiles for the NH winter 2006/07. Sensitivity of the horizontal wavelength regarding distance in spacing between the 3-points for 10° (a) and 15° (b) spatial interval are displayed.

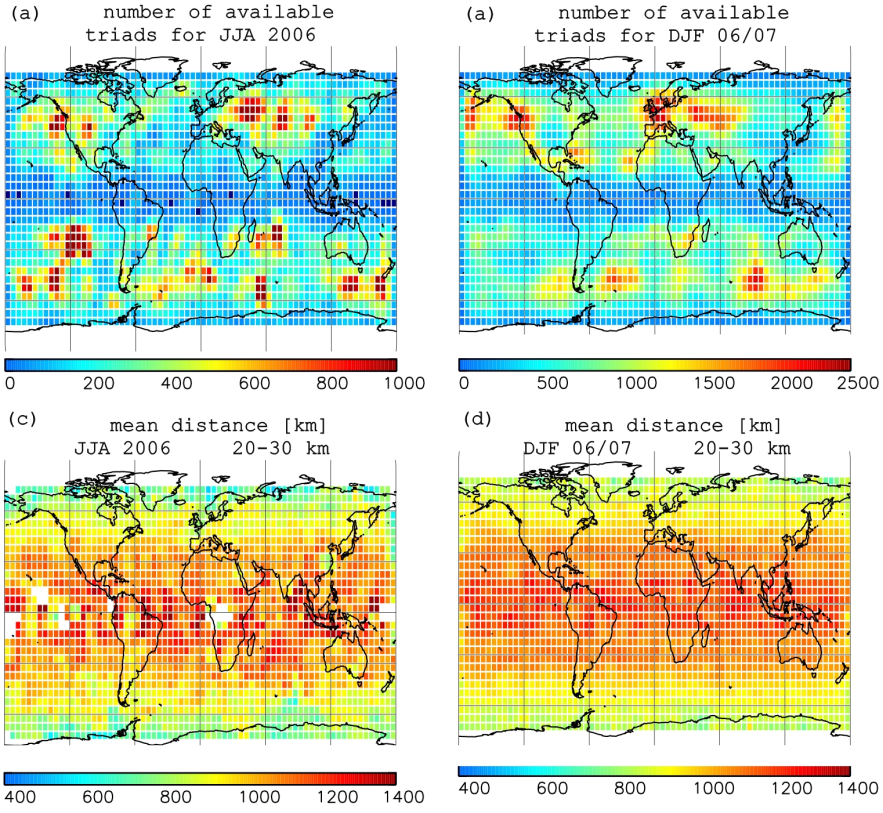

Fig. 8. Number of 3-points from COSMIC for JJA 2006 (a) and DJF 2006/07 (b) and the mean horizontal distance within the 3-points respectively (c and d) for the altitude range of 20-30 km.

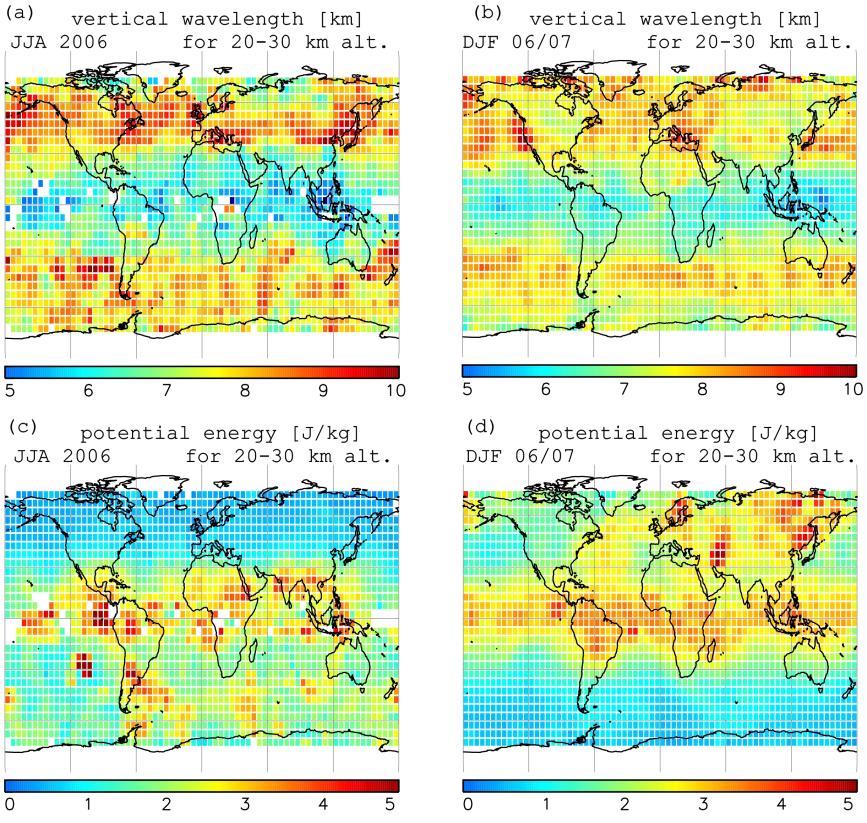

Fig. 9. Vertical wavelength derived from COSMIC for the available 3-points (JJA 2006) (a) and (DJF 2006/07) (b), and the mean potential energy distribution respectively for each season (c and d) for the altitude range of 20-30 km.

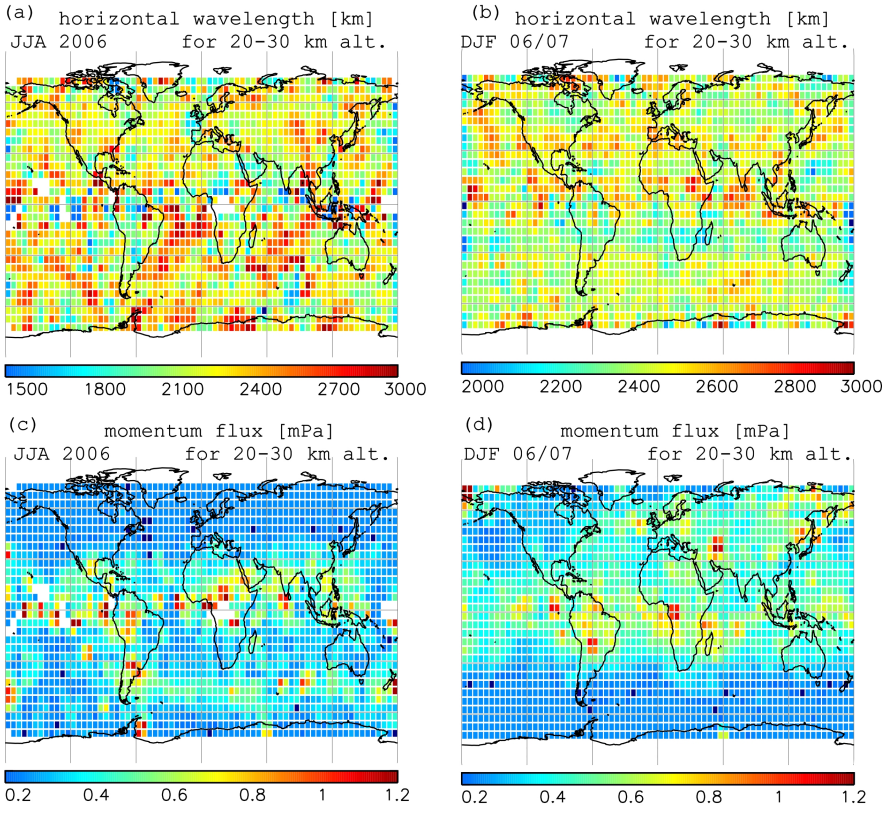

Fig. 10. Horizontal wavelength derived from 3-points of COSMIC temperature profiles for the available 3-points (JJA 2006) (a) and (DJF 2006/07) (b), and the mean momentum flux distribution respectively for each season (c and d) for the altitude range of 20-30 km.